

# Complex Wavelets for Extended Depth-of-Field: A New Method for the Fusion of Multichannel Microscopy Images

BRIGITTE FORSTER, DIMITRI VAN DE VILLE, JESSE BERENT, DANIEL SAGE, AND MICHAEL UNSER\*  
 Swiss Federal Institute of Technology Lausanne (EPFL), Biomedical Imaging Group, LIB Bât. BM,  
 CH-1015 Lausanne, Switzerland

**KEY WORDS** focal range; optical microscopy; digital image processing; image fusion; complex wavelet transform

**ABSTRACT** Microscopy imaging often suffers from limited depth-of-field. However, the specimen can be “optically sectioned” by moving the object along the optical axis. Then different areas appear in focus in different images. Extended depth-of-field is a fusion algorithm that combines those images into one single sharp composite. One promising method is based on the wavelet transform. Here, we show how the wavelet-based image fusion technique can be improved and easily extended to multichannel data. First, we propose the use of complex-valued wavelet bases, which seem to outperform traditional real-valued wavelet transforms. Second, we introduce a way to apply this technique for multichannel images that suppresses artifacts and does not introduce false colors, an important requirement for multichannel optical microscopy imaging. We evaluate our method on simulated image stacks and give results relevant to biological imaging. *Microsc. Res. Tech.* 65:33–42, 2004. © 2004 Wiley-Liss, Inc.

## INTRODUCTION

Limited depth-of-field is a common problem in biological imaging with conventional light microscopy. Often, the specimen’s profile covers more than the attainable depth-of-field. Portions of the object’s surface outside the optical plane appear defocused in the acquired image plane. This becomes worse as the magnification  $M$  increases because the numerical aperture  $NA$  increases, too:

$$M = \text{const. } NA, \quad (1)$$

$$NA = n \sin(\alpha), \quad (2)$$

and therefore the depth-of-field  $d$  becomes smaller:

$$d = \lambda / (n \sin^2(\alpha)), \quad (3)$$

where  $\lambda$  is the wavelength of the illumination,  $n$  the refractive index of the medium in front of the lens, and  $\alpha$  the angular semi-aperture on the objective side (Born and Wolf, 1987; Goldsmith, 2000).

Consequently, each acquisition will be compromised and show certain parts of the specimen in and out of focus. One common approach to image the whole specimen is by taking multiple images corresponding to different object planes. The challenge then becomes to select from each slice the area that is focused in order to reconstruct an image projection that is sharp everywhere. In this way, it is possible to extend the apparent depth-of-field without the physical limitation of the numerical aperture of the objective lens (see Fig. 1).

Numerous articles have been written on image fusion and some solutions have proven to be more efficient than others. An overview can be found in Li et al. (1995) and Valdecasas et al. (2001, 2002).

There are three different approaches for image fusion:

1. Point-based image fusion: Pixels  $p(x,y;z)$  with the same coordinates  $(x,y)$  are compared in all  $z$  images of a stack. A maximum or minimum selection rule is applied to select the slice in focus (see also Pieper and Korpel, 1983; Sugimoto and Ichioka, 1985).
2. Neighborhood-based image fusion: For selecting the slice in focus at coordinate  $(x,y)$ , a neighborhood of each pixel is taken into account. One example is the variance method, which we discuss below. Further examples may be found in Tympel (1996) and Goldsmith (2000).
3. Multiresolution-based methods: The guiding principle for this approach is the assumption that in-focus parts contain many details and thus many high-frequency components. The first multiresolution-based approaches for image fusion were provided by Burt and Kolczynski (1993) and Li et al. (1995); however, not for microscopy images.

Among the multiresolution methods, one of the better-performing is based on the wavelet transform. For this method, we propose two extensions. Basically, our approach computes the discrete *complex-valued* wavelet transform of each image slice of the object, and

Contract grant sponsor: German Academy of Natural Scientists Leopoldina; Contract grant number: BMBF-LPD 9901/8-64 (to B.F.); Contract grant sponsor: European Union’s Human Potential Program; Contract grant number: HPRN-CT-2002-00285 (to B.F.).

\*Correspondence to: Michael Unser, Swiss Federal Institute of Technology Lausanne (EPFL), Biomedical Imaging Group, LIB Bât. BM 4.134, CH-1015 Lausanne, Switzerland. E-mail: michael.unser@epfl.ch

Received 23 June 2004; Accepted in revised form 27 August 2004

DOI 10.1002/jemt.20092

Published online in Wiley InterScience (www.interscience.wiley.com).

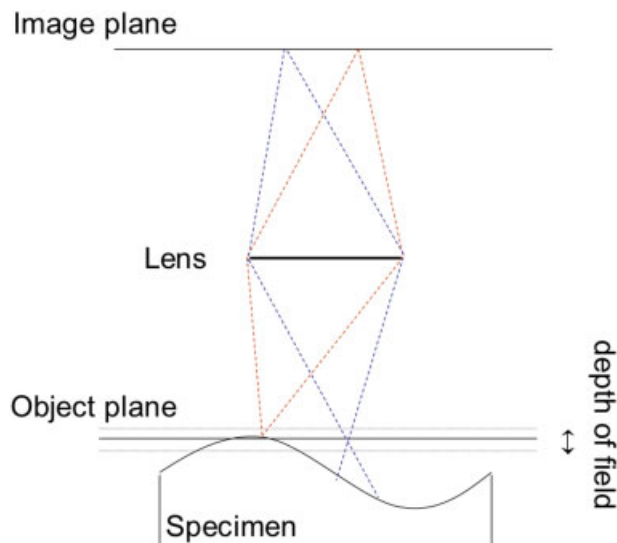


Fig. 1. Microscopic imaging system, depth-of-field. [Color figure can be viewed in the online issue, which is available at [www.interscience.wiley.com](http://www.interscience.wiley.com).]

builds up the wavelet coefficients of the composite image by a maximum-absolute-value selection rule. The final composite image is obtained after computing the inverse complex wavelet transform. For successful application to multichannel images, we propose an adapted multichannel conversion and recovery as a pre- and postprocessing step. In essence, this method compensates for the increase in dynamic range of the image obtained after fusion and avoids the introduction of false colors (Forster et al., 2004). We propose a quantitative validation procedure that allows us to compare our method with other approaches and to evaluate its performance. We also present results obtained with real specimens.

### MATERIALS AND METHODS In Focus Criterion

To extend the depth-of-field, we first have to define an in-focus criterion. Typically, an image that is in-focus has a maximal number of visible details. On the other hand, defocused images are blurred by the point-spread-function of the microscope. Therefore, we suppose that the areas of an image that are focused contain more high-frequency components than the out-of-focus areas.

Classical frequency analysis, using the Fourier transform, does not provide any spatial localization. The discrete wavelet transform, by contrast, seems to be the ideal high saliency detection, since it allows a local analysis of the image's frequency content. Unlike windowed Fourier transforms, this type of multiresolution automatically adapts to various sizes of details. Moreover, the discrete wavelet transform is nonredundant and invertible.

### Image Fusion Algorithm

The image fusion algorithm proposed in this article relies on two conditions prior to processing. The first is

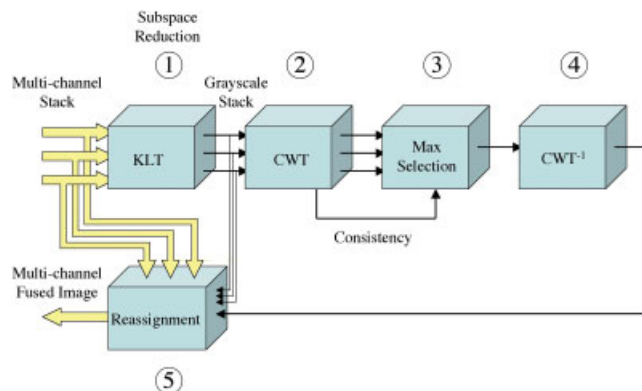


Fig. 2. Image fusion algorithm. [Color figure can be viewed in the online issue, which is available at [www.interscience.wiley.com](http://www.interscience.wiley.com).]

that the images must be aligned throughout the stack and the second is that at least the in-focus areas must be at the same magnification level. Both conditions are met if the original images are taken by a traditional light microscope with the specimen being translated along the optical axis  $z$  to obtain the slices. For best visual results, however, the whole specimen should be recorded with translation steps  $\Delta z$  smaller than the real depth-of-field. Transparent specimens may lead to visually unusual fusion results, since details at different heights in  $z$ -direction appear on the same plane. Therefore, for best performance, we suggest working with images of opaque specimens.

The flowchart outlining our procedure is shown in the block diagram of Figure 2. It consists of five steps:

1. Vector-to-scalar conversion: multichannel (e.g., color image) data is converted to one channel.
2. Complex-valued discrete wavelet transform.
3. Applying the selection rule and consistency checks.
4. Inverse complex-valued discrete wavelet transform.
5. Scalar-to-vector conversion: reassignment to obtain multichannel data.

The core of the algorithm consists of steps 2 and 4, the complex-valued discrete wavelet transform, and step 3, the selection rule and consistency checks. These steps are explained in the following sections. Steps 1 and 5 are described in the section Pre- and Postprocessing Steps.

### Complex-Valued Wavelet Transform for Image Fusion

In the past decade, the wavelet transform has become an important tool for many biomedical image analysis applications, which aim at the detection and analysis of image features (for reviews, see Aldroubi and Unser, 1996; Unser and Aldroubi, 1996; Laine, 2000). A comprehensive introduction to wavelets was written by S. Mallat (1998), who also provides an exhaustive list of references on this topic. Further aspects on wavelet theory may be found, e.g., in Daubechies (1992).

For image fusion, it is essential to detect image areas where sharp features and details are present. This can

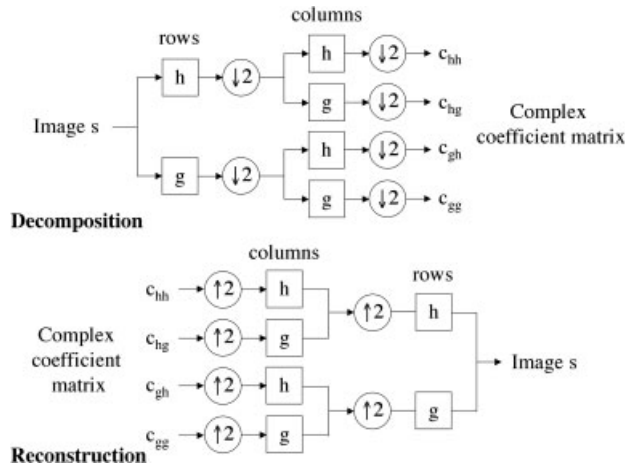


Fig. 3. Scheme of the complex-valued wavelet transform. For the decomposition of an image  $s$ , all rows and columns of the image are filtered with a low-pass filter  $h$  and a high-pass filter  $g$ , and subsampled thereafter. The resulting coefficient matrix  $c$  is complex-valued and contains coarse scale information  $c_{hh}$  resulting from the low-pass filtering, as well as detail information  $c_{hg}$ ,  $c_{gh}$ ,  $c_{gg}$ , resulting from the high-pass filtering. The reconstruction step consists of up-sampling and filtering.

be performed using the wavelet transform, which allows for the decomposition of an image into subbands that contain details of various sizes. A short review of the wavelet transform is presented in the Appendix.

The wavelet transform can yield some useful information on the underlying signal. For instance, the presence of large wavelet coefficients in some neighborhoods serves as an indication for pronounced details at this point, which in our case is characteristic for an in-focus part of the image.

The multiresolution transforms and especially the discrete wavelet transform were proposed for image fusion previously (Burt and Kolczynski, 1993; Li et al., 1995) and then refined by several authors (see Valdecasas et al., 2001, for an overview). The proposed wavelet transforms are bi- or orthonormal basis decompositions, meaning that the information in the different wavelet subbands is unique and nonredundant. Moreover, the discrete wavelet transform is a perfect reconstruction transform that has a fast algorithm (Mallat, 1998).

However, not all wavelets have the same performance. Here, we choose the complex Daubechies wavelet bases that were independently designed by Lawton (1993) and by Lina and Mayrand (1995; Lina, 1997). These yield a complex-valued wavelet transform by filtering with finite-length complex low and high pass filters,  $h$  and  $g$ , and downsampling thereafter. Figure 3 shows the scheme of the respective algorithm for 2D images.

Complex wavelet bases of various orders of smoothness are available, and thus an adjustment of the order of smoothing performed by the transform is possible. Here, we selected the complex Daubechies wavelets with four vanishing moments, i.e., of order 3, and 6/6 taps filters, because they provide an orthonormal decomposition, which is useful for an additional denoising step, and because they have an adequate smoothness.

Thus, the first step of our algorithm is to perform a 2D separable complex wavelet transform CWT:

$$CWT: s(x,y;z) \rightarrow \{c_j(n,m;z)\}_j \quad (4)$$

for each slice  $s(\cdot, \cdot, z)$  of the stack  $\{s(x,y;z)\}_z$ , which yields complex-valued coefficients  $c_j$  for each scale  $j$  and all  $z$ .

We found that the complex-valued transform adds robustness to the selection rule and consistency check algorithms. This is due to the fact that the selection operator only takes into account the absolute value of the coefficients, and keeps the phase unchanged. As mentioned in Lina (1997), the phase of the wavelet coefficient may be interpreted as the carrier of detail information, whereas the amplitude rather weights this information. Our experiments in Evaluation and Results for Simulated Date (below) confirm our observations on improved performance with the complex-valued wavelet transform.

### Selection Rule and Consistency Checks

The largest absolute value of the coefficients in the subbands correspond to sharper brightness changes and therefore to the most salient features. A good integration rule consists of selecting the slice with the largest absolute value of the wavelet coefficients at each point:

$$d_j(n,m) = c_j(n,m; \arg \max_z |c_j(n,m;z)|). \quad (5)$$

The fused transform based on the combined complex coefficients can thereafter be inverted in order to obtain a composite image. We store the number of the selected slice per pixel in a separate map  $M$ . It may be used for spatial consistency checks or topological visualization.

There are several approaches on consistency checks for the choice of the coefficients. They can be performed on the wavelet coefficients, but also on the map  $M$ , which contains the number slice the pixel is chosen.

- A typical consistency check on the wavelet coefficients is the subband consistency check: If two out of three corresponding subband coefficients are attributed to the same slice, then the third one is taken from that slice, too.
- As spatial consistency check on the map, we consider the following rule: If the majority of neighboring numbers in a  $3 \times 3$  window in the map  $M$  are from a different slice  $k \neq j$ , then the number  $M(n,m) = j$  is changed to  $M(n,m) = k$ , and the respective coefficient is adapted:  $d_{j,\text{new}}(n,m) = c_j(n,m;k)$ .

### Inverse Complex Discrete Wavelet Transform

We compute the inverse complex wavelet transform on the fused coefficient matrix to get an intermediate fused image:

$$CWT^{-1}: \{d_j(n,m)\}_j \rightarrow p(x,y). \quad (6)$$

In general, the pixels of the reconstructed image are complex numbers. We considered two schemes for mapping these back to real values: 1) Calculating the absolute value of the complex number per pixel; 2) Taking

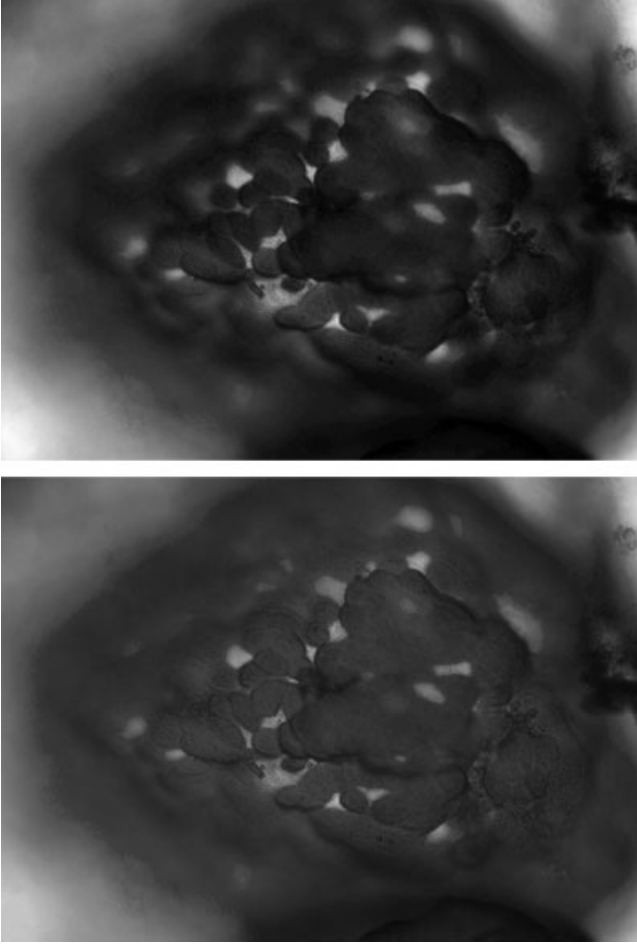


Fig. 4. One slice of a stack showing Peyer plaques from the intestine of a mouse. Multichannel conversion with principal component analysis (upper image), and with fixed weights (lower image). Principal component analysis gives more contrast.

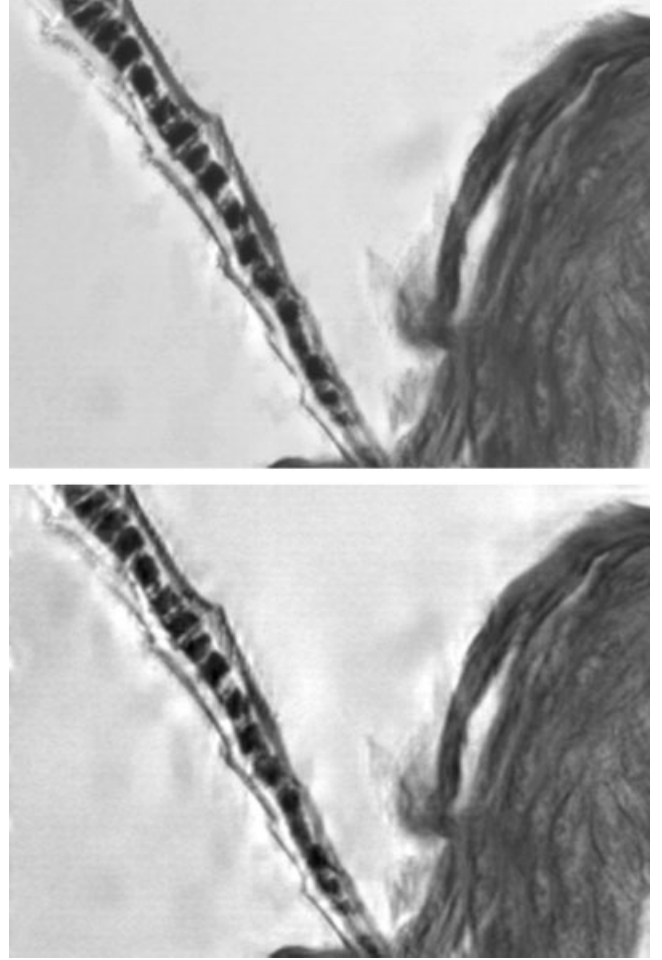


Fig. 5. Mouse epidermis. Reassignment (upper image) diminishes ringing effects (lower image).

the real part of each pixel. We found the second approach to perform better.

### Pre- and Postprocessing Steps

**Preprocessing: Multichannel Conversion.** Having at our disposal a scalar fusion method based on the wavelet transform, one would be tempted to apply the algorithm to multichannel data by treating each channel independently. Such an approach could be useful for multichannel data where the details are not correlated across channels. However, if the channels jointly contribute to details, this method will cause saturation and false colors (see also Lucchese and Mitra, 2004). Moreover, we would have to perform the whole algorithm several times, which would increase the computation time and storage space. Here, we propose instead to convert color images to grayscale in order to apply the algorithm once only.

The traditional method to perform color conversion from RGB images to grayscales consists of computing the luma, which is a fixed weighted average of the three colors (i.e.,  $Y = 0.30 \text{ Red} + 0.59 \text{ Green} +$

$0.11 \text{ Blue}$ ) (Poynton, 1996). This is a universal color to grayscale transformation that has been optimized for natural images. However, in microscopy images a particular color might be highly present (e.g., a specimen stained using a colorant), or different channels than the traditional RGB might be available (e.g., in mixed fluorescence/brightfield image acquisition).

Therefore, we apply a vector-to-scalar conversion

$$\{s^{(k)}(x,y;z)\}_k \rightarrow \{s(x,y;z)\}, \quad (7)$$

where  $s(x,y;z) = \sum_k w_k s^{(k)}(x,y;z)$  is a weighted linear combination of data coming from the  $k$  different channels. The weights are obtained from a principal components analysis (Parkkinen et al., 1989; Vrhel et al., 1994; Maloney, 1999; Ramanath et al., 2004) with the Karhunen-Loève transform (KLT). This choice corresponds to the direction in the multichannel space having maximum variance.

In this way, a predominant color will be given more weight during the subsequent fusion algorithm. The grayscale images created preserve more saliency and contrast than by simply using fixed weights (see Fig. 4).

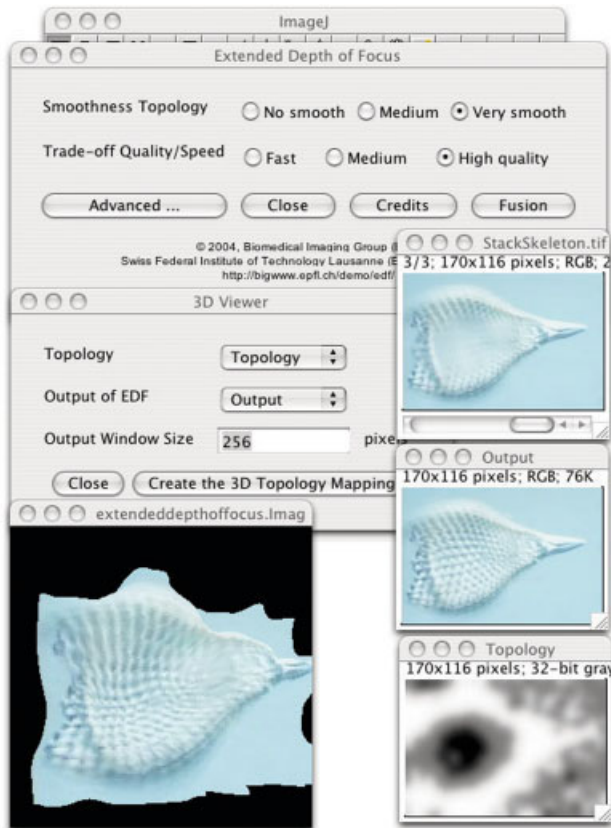


Fig. 6. Screenshot of our software package, which is freely available as a plug-in for the ImageJ Java Image Processing Framework.

**Postprocessing: Reassignment.** Fusion in the wavelet domain yields results that are “nonconvex” combinations of the pixel values of the input images; a consequence of retaining the maximal absolute value coefficient. For typical images,  $\sim 30\%$  of the pixels are over or under the original dynamic range of all images. Such an increase of dynamic range boosts the global energy of the image, the noise level, and the amount of saturation.

To at least avoid the nonconvexity errors, we propose a “reassignment” algorithm that selects the closest available value according to the grayscale data. Multichannel reassignment for each channel  $k$  can be expressed as:

$$q^{(k)}(x, y) = s^{(k)}(x, y; \arg \min_z |p(x, y) - s(x, y; z)|). \quad (8)$$

This procedure eliminates outliers and diminishes ringing effects (see Fig. 5). Moreover, it can be applied to “restore” the multichannel pixel data, without false color effects. In this way, the final image is made up of (multichannel) pixel values that are present in the initial data.

### Software Package

We implemented our method in Java as an ImageJ plug-in. The ImageJ general-purpose image processing package is a widely used multiplatform public domain

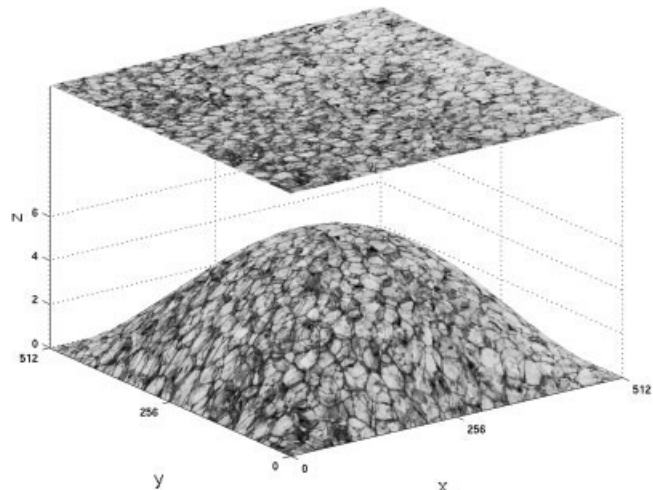


Fig. 7. Construction of a simulated data stack by projecting a Brodatz texture on a surface. The volume is discretized using linear interpolation along the  $z$ -direction. To simulate the optical system, the volume is convolved with a Gaussian blur for each slice with increasing width as defocus increases.

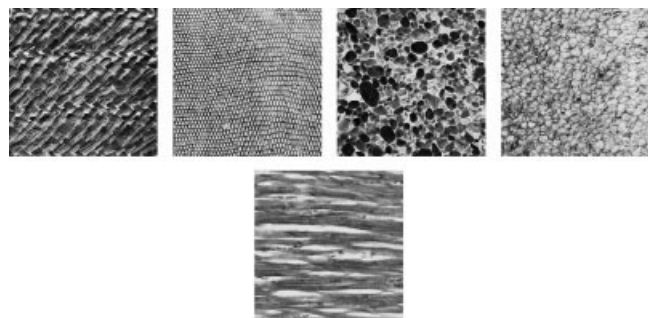


Fig. 8. Brodatz textures (upper row) and histological tissue used for the generation of the artificial stacks.

software for the analysis of biological images. Our algorithm is freely available and can be downloaded from our web site (<http://bigwww.epfl.ch/demo/edf/>). It allows the fusion of a stack of images with a single mouse click (Fig. 6).

The software assumes that the images in the stack are registered, which can easily be attained by fixing the specimen on the object table and moving the object table in the axial direction for each image acquisition. For best results, the step between two acquired images should be less than the depth-of-field. The software is suited for multichannel data. It converts color stacks into grayscale stacks, applies the complex wavelet transform for fusion in the wavelet domain, and performs an optional denoising step and reassignment. The resulting fused image can be easily stored in various image formats by the standard methods supplied by the ImageJ software.

### RESULTS

In this section, we compare the performance of our complex wavelet method with more standard schemes, including the classical real-valued wavelets and the

TABLE 1. Average performance gain of the real and the complex wavelet method with preprocessing and consistency checks compared to the variance method

Performance gain compared to variance method	Spline 3	Complex Daubechies 6	Complex Daubechies 6 compared to spline 3
No manipulations	2.49 dB	3.21 dB	0.72 dB
Reassignment	2.87 dB	3.51 dB	0.64 dB
Spatial check	3.55 dB	3.67 dB	0.12 dB
Spatial check, reassignment	3.74 dB	3.89 dB	0.15 dB
Subband check	4.14 dB	4.50 dB	0.36 dB
Subband check, reassignment	4.33 dB	4.70 dB	0.37 dB

The experiments were performed on four artificial stacks generated with Brodatz textures. The left columns give the average difference of the SNRs with respect to the variance method. The right column gives the SNR's average differences of the complex wavelet method and the real one. The SNRs of both wavelet methods without manipulations range between 23.7–26.9 dB.

TABLE 2. Average performance gain of the real and the complex wavelet method with preprocessing and consistency checks compared to the variance method

Performance gain compared to variance method for the experiment with histologic tissue	Variance method	Spline 3 compared to variance method	Complex Daubechies 6 compared to variance method	Complex Daubechies 6 compared to spline 3
No manipulations	26.79 dB	−0.58 dB	0.64 dB	1.22 dB
Reassignment		0.26 dB	1.16 dB	0.90 dB
Spatial check		−0.19 dB	0.89 dB	1.08 dB
Spatial check, reass.		0.54 dB	1.48 dB	0.94 dB
Subband check		2.24 dB	2.95 dB	0.71 dB
Subb. check, reass.		2.54 dB	3.41 dB	0.87 dB

The experiments were performed on an artificial stack generated from histological tissue.

variance method. First, we evaluate our method using simulated microscopy data, which allows us to compare the reconstructed image with the ground truth. Next, we present results using real-world data.

### Classical Approach

The variance method is based on the assumption that the larger variations of intensity occur in the regions of the image that are in-focus. The variance over a  $3 \times 3$  window is calculated in order to determine whether the center pixel is in a focused area. The pixel along the z-axis with the highest variance is chosen for the composite image. This algorithm has the advantage of computational simplicity (Yeo et al., 1993).

### Evaluation and Results for Simulated Data

For testing purposes, five simulated stacks were constructed as illustrated in Figure 7. Four different Brodatz textures (D18, D22, D23, D112) (Brodatz, 1966) and an example of histological tissue (cam21ih) (Slo-mianka, 2003) (Fig. 8) were mapped onto a surface and discretized using linear interpolation along the z-direction. Next, each slice was convolved by a Gaussian point spread function (PSF) with increasing width as the defocus distance increases. The sum of the filters' coefficients for the Gaussian PSF at each focal distance is normalized, which corresponds to the case of Köhler illumination.

Gaussian PSFs are often used as an approximation in situations where the physical PSF is difficult to obtain (Kayargadde and Martens, 1994; Elder and Zucker, 1998). In particular, the theoretical physical PSF depends on many parameters that are typically unknown for conventional light microscopy; e.g., the light source's spectrum, the distance of the specimen's surface to the coverslip (Gibson and Lanni, 1991), and the through-focus image formation for a specimen

whose thickness cannot be neglected (Oliva et al., 1999).

We compared the variance method, the real wavelet method, and the complex wavelet method. We used the real orthonormal spline wavelet of degree 3 and the 6/6 tap complex Daubechies wavelet, since they have the same number of vanishing moments. Moreover, we evaluated the influence of reassignment and of the consistency checks. For all experiments we measured the signal-to-noise-ratio (SNR) with respect to the ground truth. The results are given in Table 1 expressed as SNR gain, i.e., the differences in the SNR, with respect to the variance method. We found that for Brodatz textures both wavelet methods outperform the variance method. The quality of the output image of the variance method is quite poor. Problems occur especially when the focused area contains homogeneous parts; often, artificial details are introduced. The complex wavelet approach outperforms the real wavelet method by about 0.7 dB. Reassignment adds about 0.3 dB for both wavelet methods. Consistency checks improve the quality of the result, especially when they are combined with reassignment. The subband consistency check, in particular, gives a good improvement.

For the histological tissue experiment, the results are given in Table 2. In this case, the real wavelet transform without postprocessing performed worse than the variance method. Combined with reassignment and consistency checks, however, the real wavelet transform gives good fusion results. The complex wavelet transform performs best with and without postprocessing.

However, both consistency checks turned out to be very costly with respect to storage space and computation time. For the processing of real microscopic stacks (typical resolution of  $1996 \times 1450$ , about 40 images),

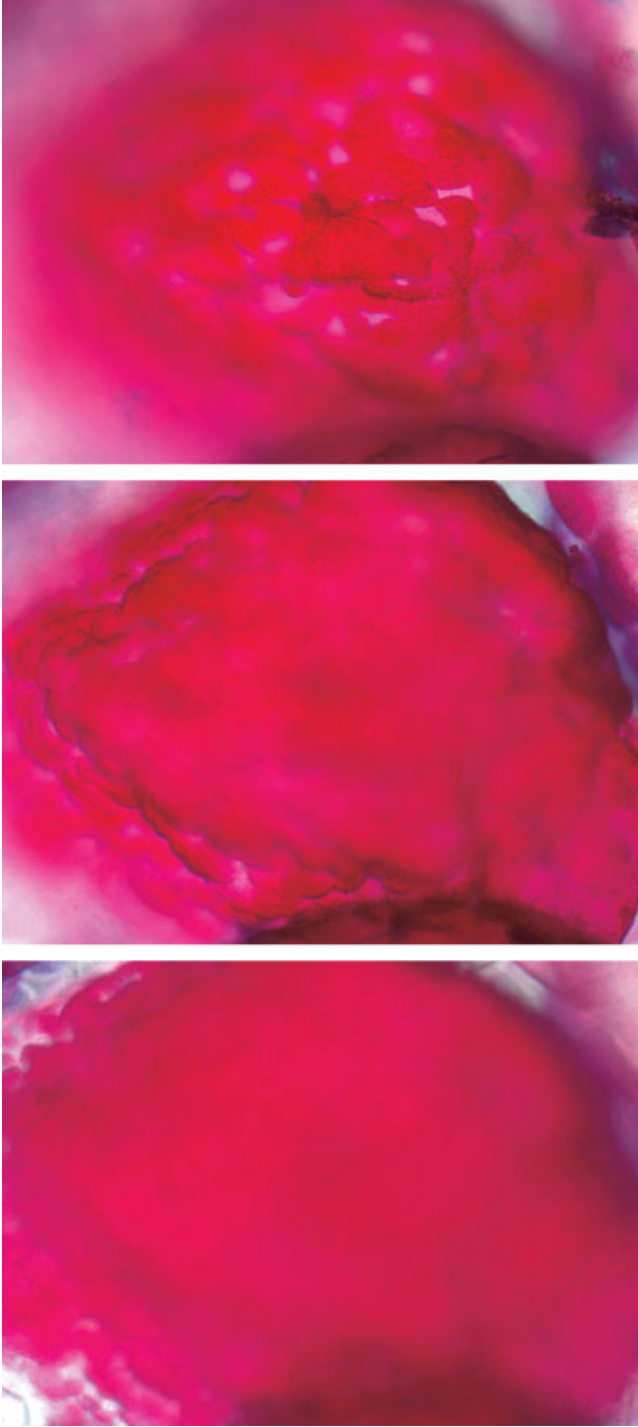


Fig. 9. Some samples from the original stack imaging the Peyer plaques of the intestine of a mouse.

we therefore set them aside and perform the complex wavelet method with reassignment.

### Results for Real Specimens

We discuss our results on two examples. The first is a stack of images showing Peyer plaques from the

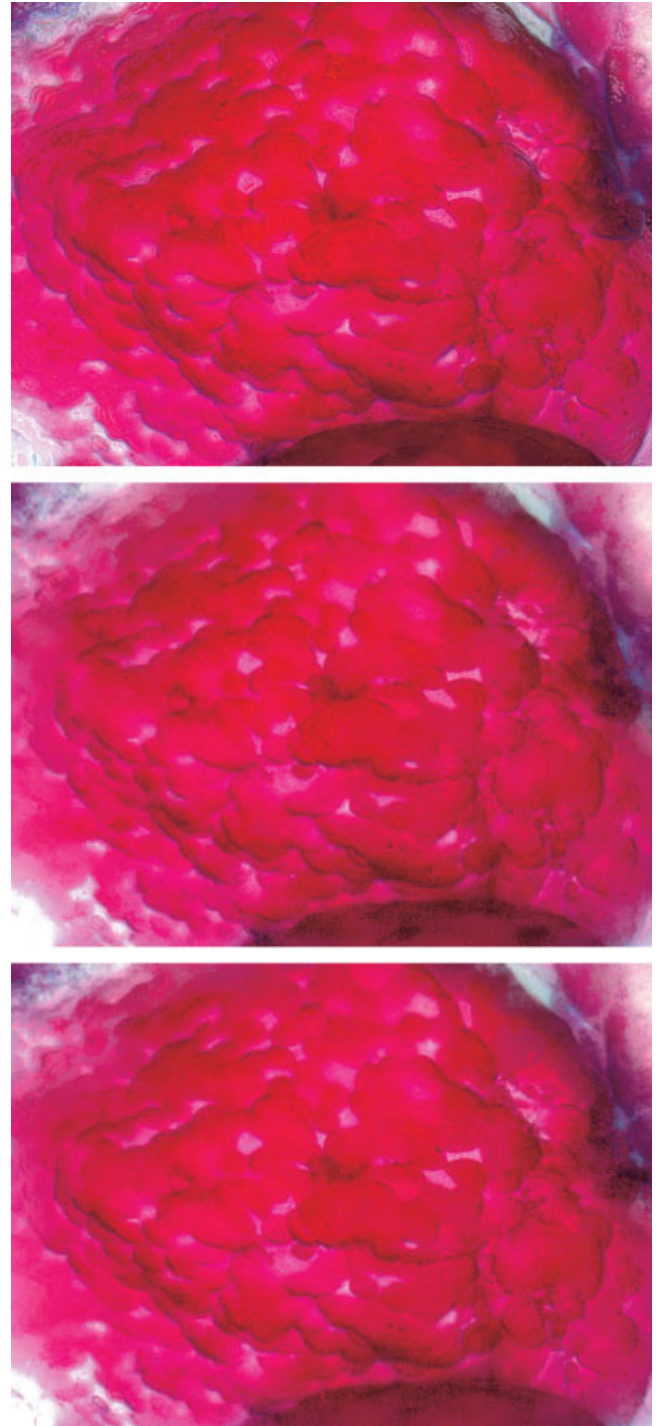


Fig. 10. The variance method (upper image), the real wavelet method (center), and the complex wavelet method (lower image) with reassignment. The variance method produces artificial patterns in the boundary regions and the basins of the specimen. These artifacts do not appear in images fused with the wavelet methods. The complex wavelet method preserves edges and details more clearly, especially in the boundary regions.

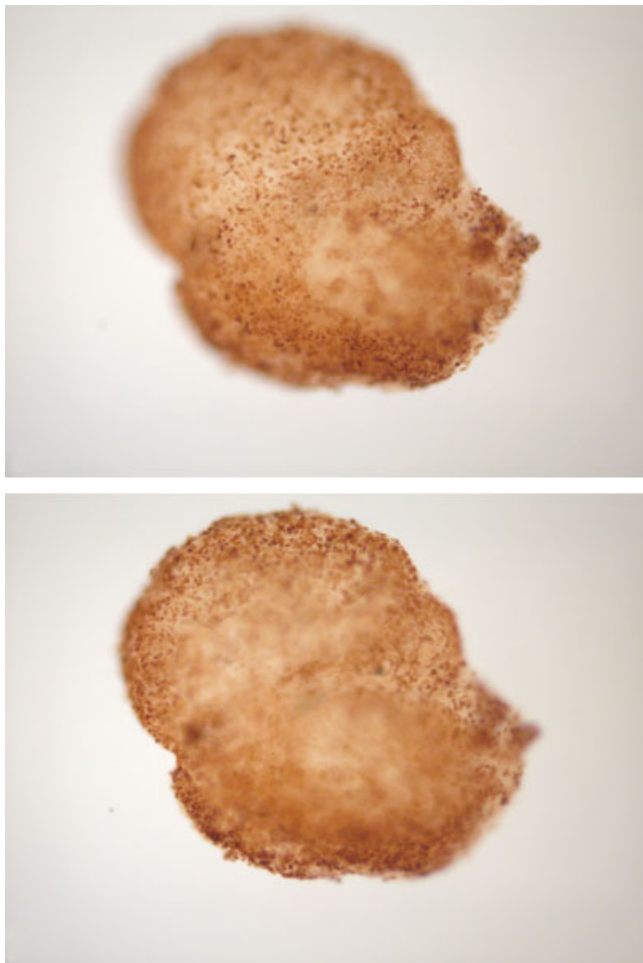


Fig. 11. Some samples from the original stack imaging a pancreatic burgeon. The specimen is stained with peroxidase.



Fig. 12. Image fusion results for the pancreas stack: The variance method (upper image), the real wavelet method (center), and the complex wavelet method (lower image) with reassignment. Also in this case, the complex wavelet method outperforms the other methods.

intestine of a mouse. Samples from the original Peyer plaques stack are shown in Figure 9. The images were taken with a Zeiss objective 40x/NA 0.75 with no immersion. The mountant medium is Citifluor, a medium with 50% PBS and 50% glycerol. The physical dimension of the object is  $100 \times 100 \times 50$  mm. A Jenoptik ProgRes camera with a sensor CCD of  $8.5 \times 6.4$  mm and a resolution of  $1996 \times 1450$  pixels was used. The specimen is strongly stained with a red colorant.

The second stack shows images of a pancreatic burgeon of approximate size  $300 \times 300 \times 300$  mm. The sample is stained with peroxidase. The images were taken with a Zeiss objective 10x/NA 0.3. The z-distance between subsequent images is 20 mm. The resolution is  $1996 \times 1450$  pixels. Some sample images from the stack are shown in Figure 11.

In Figures 10 and 12 the fusion results for the example stacks are shown. For real-world data, we found that the complex wavelet method with reassignment proposed in this article outperforms the classical fusion method in terms of subjective visual quality. It gives more details in the boundary regions than the real wavelet method and the variance method. Moreover,

both wavelet methods do not introduce artificial details as the variance method does (Figs. 10, 12).

### DISCUSSION AND CONCLUSION

We present a new method to extend the depth-of-field of microscopic images. The strong point of our method is its simplicity: The use of complex-valued wavelets, and pre- and postprocessing steps such as a smart multichannel conversion and consistency checks, as well as reassignment, enhance the quality of the resulting fused image.

Our method has several practical advantages over other methods:

We do not need knowledge of the imaging parameters, such as the point spread function or microscope parameters. In tests, we found that, although our method does not include imaging parameters, it is more stable than classical deconvolution with an estimated point spread function (Biemond et al., 1990).

With our fusion method, no special imaging techniques or hardware are needed to extend the depth of field, as, e.g., phase masks (Cathey and Dowski, 2002). We get high-quality results even with image stacks taken with standard light microscope equipment.

The multichannel conversion ensures that saliencies from all channels are kept in proportion to their strength. This preserves contrast, reduces artifacts, and allows fusion of multichannel data by one single fusion step.

Using both simulated microscopy data and images acquired from real-world specimens, we showed that our choice of a complex wavelet transform outperforms real wavelets and the variance method. The introduced phase information yields stability for the consistency checks and better preserves image details during the fusion step.

Reassignment assures that the pixels from the original image stack are used to represent the fused image. Thus, the original multichannel data is preserved, which is important for the evaluation and biological interpretation of the fused images. Moreover, artifacts are suppressed.

However, our method has some requirements for the image stacks. First, the magnification should be constant for all images of the stack. Otherwise, there may be artifacts generated by details appearing at various sizes. Second, the specimen should be nonreflective and nontransparent. This ensures that the in-focus point for each  $z$ -position is unique. Third, for best color reproduction the illumination should be approximately constant. This can easily be reached with Köhler illumination. For best results, the  $z$ -distance between subsequent images of the stack should be smaller than the depth-of-field. This ensures that all parts of the specimen appear in focus on some image of the stack.

Since we use a maximum selection rule for the image fusion in the wavelet domain, the noise level might be enhanced. Therefore, a wavelet denoising operator (Donoho and Johnstone, 1994; Lina, 1997) can be applied to the fused coefficient matrix. Depending on the smoothness of the chosen wavelet, the resulting fused image may appear slightly smoothed.

Our ImageJ plugin is used in practice by biologists at the ISREC cancer research facility in Lausanne. We believe that it might be helpful for biologists in other

research laboratories working with microscopy images, which is the reason why we are making our software freely available on the web.

The algorithm can be applied to visualize and present light microscopy images. Another application is the reconstruction of a sharp DIC (differential interference contrast) image, containing structural information of a biological specimen that is superposed with fluorescence images. As an extension, we are working on improving the height map for an estimation of an elevation surface and for 3D reconstruction.

### ACKNOWLEDGMENTS

The images are courtesy of Jelena Mitic, Laboratoire d'Optique Biomédicale at EPF Lausanne, Nathalie Garin and Claude Bonnard, Microscopy-Imaging-Morphology Core Facility at the ISREC Lausanne, and Zeiss.

### REFERENCES

- Aldroubi A, Unser M (eds.). 1996. Wavelets in medicine and biology. Boca Raton, FL: CRC Press.
- Biemond J, Lagendijk RL, Mersereau RM. 1990. Iterative methods for image deblurring. *Proc IEEE* 78:856–883.
- Born M, Wolf E. 1987. Principles of optics. New York: Pergamon Press.
- Brodatz P. 1966. Textures — a photographic album for artists and designers. New York: Dover.
- Burt PJ, Kolczynski RJ. 1993. Enhance image capture through fusion. Berlin: IEEE. p 173–182.
- Cathey WT, Dowski ER. 2002. New paradigm for imaging systems. *Appl Opt* 41:6080–6092.
- Daubechies I. 1992. Ten lectures on wavelets. Philadelphia: SIAM.
- Donoho DL, Johnstone IM. 1994. Ideal spatial adaptation by wavelet shrinkage. *Biometrika* 81:425–455.
- Elder J, Zucker S. 1998. Local scale control for edge detection and blur estimation. *IEEE Trans Pattern Anal Machine Intell* 20:699–716.
- Forster B, Van De Ville D, Berent J, Sage D, Unser M. 2004. Extended depth-of-focus for multi-channel microscopy images: a complex wavelet approach. Arlington VA: IEEE.
- Gibson SF, Lanni F. 1991. Experimental test of an analytic model of aberration in an oil-immersion objective lens used in 3D light microscopy. *J Opt Soc Am A* 8:1601–1613.
- Goldsmith NT. 2000. Deep focus; a digital image processing technique to produce improved focal depth in light microscopy. *Image Anal Stereol* 19:163–167.
- Kayargadde V, Martens J-B. 1994. Estimation of edge parameters and image blur using polynomial transforms. *Graph Models Image Proc* 56:442–461.
- Laine AF. 2000. Wavelets in temporal and spatial processing of biomedical images. *Annu Rev Biomed Eng* 2:511–550.
- Lawton W. 1993. Applications of complex valued wavelet transforms to subband decomposition. *IEEE Trans Signal Proc* 41:3566–3568.
- Li H, Manjunath BS, Mitra SK. 1995. Multisensor image fusion using the wavelet transform. *Graph Models Image Proc* 57:235–245.
- Lina J-M. 1997. Image processing with complex Daubechies wavelets. *J Math Imag Vis* 7:211–223.
- Lina J-M, Mayrand M. 1995. Complex Daubechies wavelets. *Appl Computat Harmonic Anal* 2:219–229.
- Luchese L, Mitra SK. 2004. A new class of chromatic filters for color image processing. Theory and applications. *IEEE Trans Image Proc* 13:534–548.
- Mallat S. 1989. A theory for multiresolution signal decomposition: the wavelet representation. *IEEE Trans Pattern Recog Machine Intell* 11:674–693.
- Mallat S. 1998. A wavelet tour of signal processing. New York: Academic Press.
- Maloney L. 1999. Physics based approaches to modeling surface color perception. In: Gegenfurtner K, Sharpe L, editors. Color vision, from genes to perception. Cambridge, UK: Cambridge University Press. p 387–416.
- Oliva MA, Bravo-Zanoguera M, Price JH. 1999. Filtering out contrast reversals for microscopy autofocus. *Appl Opt* 38:638–646.
- Parkkinen J, Hallikainen J, Jaaskelainen T. 1989. Characteristic spectra of Munsell colors. *J Opt Soc Am A* 6:318–322.

- Pieper RJ, Korpel A. 1983. Image processing for extended depth of field. *Appl Opt* 22:1449–1453.
- Poynton C. 1996. A technical introduction to digital video. New York: John Wiley & Sons.
- Ramanath R, Keuhni RG, Snyder WE, Hinks D. 2004. Spectral spaces and color spaces. *Color Res Appl* 29:29–37.
- Slomianka L. 2003. Blue histology. University of Western Australia, School of Anatomy and Human Biology.
- Sugimoto SA, Ichioka Y. 1985. Digital composition of images with increased depth of focus considering depth information. *Appl Opt* 24:2076–2080.
- Tympel V. 1996. A new high level image capture system for conventional light microscopy. In: Kim Y, editor. *SPIE*. p 529–536.
- Unser M, Aldroubi A. 1996. A review of wavelets in biomedical applications. *Proc IEEE* 84:626–638.
- Valdecasas AG, Marshall D, Becerra M, Terrero JJ. 2001. On the extended depth of focus algorithms for bright field microscopy. *Micron* 32:559–569.
- Valdecasas AG, Marshall D, Becerra JM. 2002. Extended depth-of-focus algorithms in brightfield microscopy. *Eur Microsc Anal* 79:15–17.
- Vrhel M, Gershon R, Iwan L. 1994. Measurement and analysis of object reflectance spectra. *Color Res Appl* 19:4–9.
- Yeo TTE, Ong SH, Jayasooriah, Sinniah R. 1993. Autofocusing for tissue microscopy. *Image Vis Comput* 11:629–639.

## APPENDIX

### Wavelet Transform, a Short Review

We consider the space  $L^2(R)$ , which can be interpreted as the space of all functions  $f: R \rightarrow C$ , which have finite energy. A multiresolution analysis of  $L^2(R)$  is a sequence of closed subspaces:

$$\{0\} \subseteq \dots \subseteq V_{-1} \subseteq V_0 \subseteq V_1 \subseteq \dots \subseteq L^2(R), \quad (9)$$

that satisfy the following conditions:

- (i) In the limit, these spaces generate the whole space  $L^2(R)$ ; i.e., the closure:

$$\text{cl}(\cup_{j \in \mathbb{Z}} V_j) = L^2(R). \quad (10)$$

This means that any  $f \in L^2(R)$  can be represented as a series of functions from the union of spaces  $(\cup_{j \in \mathbb{Z}} V_j)$ .

- (ii) The spaces  $V_j$  decompose  $L^2(R)$  completely; i.e., only the function  $f = 0$  is element of all  $V_j$  and thus element of their intersections:

$$\cap_{j \in \mathbb{Z}} V_j = \{0\}. \quad (11)$$

- (iii) The spaces  $V_j$  are related through a scaling relation:

$$f(x) \in V_j \quad \text{if and only if} \quad f(2x) \in V_{j+1}. \quad (12)$$

- (iv) The spaces  $V_j$  are translation invariant:

$$f(x - k) \in V_0 \quad \text{if and only if} \quad f(x) \in V_0. \quad (13)$$

- (v) Moreover,  $V_0$  has a basis consisting of the translates of one single function  $\varphi$ , the so-called scaling function.

Multiresolution aims at decomposing:

$$L^2(R) = V_0 \oplus \sum_{j \geq 0} W_j \quad (14)$$

into a coarse scale space  $V_0$  and detail spaces  $W_j$ , where  $V_{j+1} = V_j \oplus W_j$  for all  $j \in \mathbb{Z}$ . This fact allows the interpretation that  $V_{j+1}$  contains finer information than  $V_j$ . The difference signal (or detail) is included in the space  $W_j$ . A function  $f \in L^2(R)$  can be decomposed in its coarse part and details of various sizes by projecting it onto the spaces  $V_0$  and  $W_j$ ,  $j \geq 0$ . To find such decomposition explicitly, basis functions of these spaces are needed. It is well known (see, e.g., Mallat, 1998, and references therein) that there exist scaling functions  $\varphi$  and wavelets  $\psi$  such that:

$$V_j = \text{cl span}\{\varphi_{j,k} = 2^{j/2}\varphi(2^jx - k); k \in \mathbb{Z}\} \quad (15)$$

and

$$W_j = \text{cl span}\{\psi_{j,k} = 2^{j/2}\psi(2^jx - k); k \in \mathbb{Z}\} \quad (16)$$

are both spanned by translates of dilated versions of these functions. The scaling function and the wavelet may be chosen such that  $\{\varphi_{j,k}\}_k$  and  $\{\psi_{j,k}\}_k$  form orthonormal families. It should be noted that there also exist biorthogonal wavelet bases that are not orthonormal but essentially as easy and as convenient to work with (Mallat, 1998). Since  $V_1 = V_0 \oplus W_0$ , we can express any function  $f \in V_0$  as:

$$f = \sum_k \langle f, \varphi_{-J,k} \rangle \varphi_{-J,k} + \sum_{j=-J}^{-1} \sum_k \langle f, \psi_{j,k} \rangle \psi_{j,k}, \quad (17)$$

where the first term on the right-hand side represents the low pass part, and the second term is a sum of residuals from scale  $-J$  to  $-1$ .

Using the two-scale relation we find an iterative scheme for calculating the coefficients:

$$\langle f, \varphi_{j-1,k} \rangle = 2^{1/2} \sum_k h^*_{k-2n} \langle f, \varphi_{j,k} \rangle, \quad (18)$$

$$\langle f, \psi_{j-1,k} \rangle = 2^{1/2} \sum_k g^*_{k-2n} \langle f, \varphi_{j,k} \rangle, \quad (19)$$

where  $*$  denotes the complex conjugate of corresponding series  $h = \{h_k\}_{k \in \mathbb{Z}}$  and  $g = \{g_k\}_{k \in \mathbb{Z}}$ . This leads to the fast wavelet decomposition algorithm (Mallat, 1989). Practically, this means that the coefficients can be calculated quite simply by filtering with low and high pass filters  $h$  and  $g$ , and downsampling thereafter. For image processing, we use tensor products to extend the multiresolution scheme to 2D.